

Minerva Access is the Institutional Repository of The University of Melbourne

Author/s:

Mubarak, SSM;Malcolm, TR;Brown, HG;Hanssen, E;Maher, MJ;McColl, G;Jameson, GNL

Title:

Biochemical Characterization of *Caenorhabditis elegans* Ferritins

Date:

2023-05-02

Citation:

Mubarak, S. S. M., Malcolm, T. R., Brown, H. G., Hanssen, E., Maher, M. J., McColl, G. & Jameson, G. N. L. (2023). Biochemical Characterization of *Caenorhabditis elegans* Ferritins. *Biochemistry*, 62 (9), pp.1484-1496. <https://doi.org/10.1021/acs.biochem.3c00005>.

Persistent Link:

<https://hdl.handle.net/11343/332872>

Biochemical Characterization of *Caenorhabditis elegans* Ferritins

Sanjeedha S. M. Mubarak,^a Tess R. Malcolm,^a Hamish G. Brown,^b Eric Hanssen,^{b,c} Megan J. Maher,^{a,*} Gawain McColl,^{d,*} Guy N. L. Jameson^{a,*}

^a School of Chemistry, Bio21 Molecular Science and Biotechnology Institute, The University of Melbourne, 30 Flemington Road, Parkville, VIC 3010, Australia.

^b Ian Holmes Imaging Centre, Bio21 Molecular Science and Biotechnology Institute, University of Melbourne, Parkville, VIC 3010, Australia.

^c Department of Biochemistry and Pharmacology and ARC Industrial Transformation Training Centre for Cryo-electron Microscopy of Membrane Proteins, The University of Melbourne, 30 Flemington Road, Parkville, VIC 3010, Australia.

^d Florey Institute of Neuroscience and Mental Health, The University of Melbourne, 30 Royal Parade, Parkville, VIC, 3052, Australia

Correspondence: guy.jameson@unimelb.edu.au
 gawain.mccoll@florey.edu.au
 megan.maher@unimelb.edu.au

Abstract: The nematode *C. elegans* contains genes for two types of ferritin (*ftn-1* and *ftn-2*) that express FTN-1 and FTN-2. We have expressed and purified both proteins and characterized them by X-ray crystallography, cryo-electron microscopy, transmission electron microscopy, dynamic light scattering and kinetically by oxygen electrode and UV-vis spectroscopy. Both show ferroxidase activity, but although they have identical ferroxidase active sites, FTN-2 is shown to react approximately 10 times faster than FTN-1, with L-type ferritin character over longer time periods. We hypothesize that the large variation in rate may be due to differences in the 3- and 4-fold channels into the interior of the protein 24-mer. FTN-2 is shown to have a wider entrance into the 3-fold channel than FTN-1. Additionally, the charge gradient through the channel of FTN-2 is more pronounced, with Asn and Gln residues in FTN-1 replaced by Asp and Glu residues in FTN-2. Both FTN-1 and FTN-2 have an Asn residue near the ferroxidase active site that is a Val in most other species, including human H ferritin. This Asn residue has been observed before in ferritin from the marine pennate diatom *Pseudo-mitochondria multiseries*. By replacing this Asn residue with a Val in FTN-2, we show that the reactivity decreases over long timescales. We therefore propose that Asn106 is involved in iron transport from the ferroxidase active site to the central cavity of the protein.

Introduction

The nematode *Caenorhabditis elegans* was first introduced as a model organism in the 1970s [1]. Starting with determination of the structure of the nervous system and establishing the genome sequence of the organism, today, *C. elegans* is used for a vast range of studies of biological processes such as early development, neurobiology, cell signaling and ageing [1-3]. These studies have revealed a strong correlation in cellular pathways between *C. elegans* and mammals that has led to major discoveries such as programmed cell death and RNA interference [4-6]. The ability to manipulate the genome of this model organism allows the action-response correlation of the complex pathways involved in iron metabolism to be understood.

The genes *ftn-1* and *ftn-2* encode two types of ferritins in *C. elegans*, FTN-1 and FTN-2 respectively. These genes have been characterized by monitoring transcription levels in the organism and tissue specific expression in response to different iron exposure levels in both wild-type and mutant organisms [7, 8]. Initial in-roads into understanding iron-ferritin interactions have been made but biochemical characterization of *C. elegans* ferritins has not yet been achieved [9, 10].

Ferritin, consisting of 24 protein subunits in a spherical architecture, creates an interior cavity that permits thousands of iron atoms in the form of a ferric oxy-hydroxide to mineralize [11]. It is involved in iron storage, iron release and thereby detoxification of cellular iron [12]. While bacterial and archaeal ferritins are often homopolymers [13, 14], eukaryotic ferritins are heteropolymers of a mixture of either H (heavy chain) and L (light chain) [14, 15] or H, L and M (medium chain) subunits [16]. Iron(II), which otherwise can catalyze the formation of reactive oxygen species that damage cellular organelles [17, 18] is protected within ferritin. First, iron(II) translocates through channels that penetrate the external cage to reach two iron binding sites at what is called the ferroxidase center, where it is bound and its oxidation by reaction with molecular oxygen is catalyzed, resulting in the formation of Fe(III) mineral precursors. These ferroxidase sites are present in H and M subunits of eukaryotic ferritin heteropolymers [19, 20] and all subunits of bacterial and archaeal homopolymers. In contrast, the light chain subunits which lack the ferroxidase center, facilitate nucleation of the iron(III) mineral core through a specific patch of carboxylate side chains [21, 22] on the inner surface.

The iron coordinating residues of the two iron binding sites, Fe_A and Fe_B, are conserved across phyla [20, 23, 24]. Regardless of these highly conserved catalytic sites through which, according to current models, a μ -oxo-bridged diferric species is produced, dissimilar kinetics and mechanistic details have been observed between ferritins. For example, the catalytic oxidation at the ferroxidase center proceeds through a μ -1,2-peroxo diferric intermediate in human heavy chain ferritin (HuHF) [20] and bullfrog M ferritin (BfMF) [25] while cyanobacterial ferritin (SynFtn) utilizes a different mechanism where a one-electron reduction produces a mixed-valent Fe(II)/Fe(III) which eventually oxidizes to the oxo-bridged Fe(III) dimer [26]. Differences in the models describing displacement of oxidized species from the ferroxidase sites [27, 28] and differences in the end product, whether multiple oxo(hydroxo) dimers or clusters are formed [29], have all been proposed. The diversity in published data shows the inability to assign a single mechanism that explains the catalytic oxidation of all ferritins, although this has been proposed [20].

These extensive *in vitro* enzymological studies have greatly assisted our understanding of iron storage mechanisms, but important questions remain. Exploring ferritins from organisms across the phylogenetic tree may allow further understanding of the reasons behind the observed differences in the kinetics and mechanisms between ferritins. We proposed to study ferritins in *C. elegans* to corroborate details of the ferroxidase mechanism that have thus far only been proposed through sequence alignment.

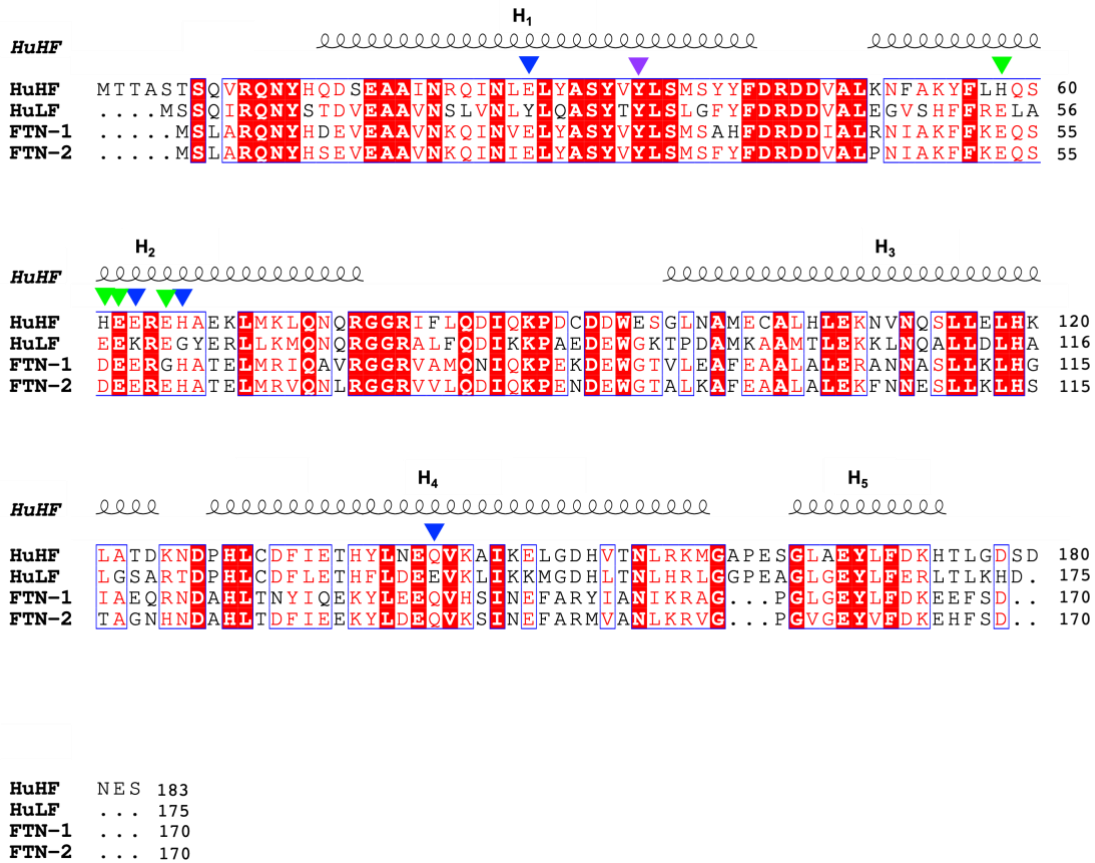


Figure 1: Structure-based sequence alignment of *C. elegans* FTN-1 and FTN-2 (79% identity), and Human H and L ferritins. *C. elegans* FTN-1 (PDB ID: 7USN) and FTN-2 (PDB ID: 7URH) structures were compared with human H ferritin (HuHF UniProtKB P02794, PDB ID: 1FHA) and human L ferritin (HuLF, UniProtKB P02792, PDB ID: 2FFX) structures. The conserved ferroxidase site residues are marked by a blue triangle and the purple triangle indicates the highly conserved tyrosine residue in the vicinity of the ferroxidase center. The green triangles indicate the putative nucleation site residues according to the tri-iron(III) cluster bound X-ray crystal structure of HuLF [21]. The alignment was performed using Superpose [30] and the figure was generated using ESPrnt 3.0 [31]. Residue numbers are indicated on the right.

Experimental elucidation of the mechanism of iron mineralization is vital to understanding the role of FTN-1 and FTN-2, despite the presence of a proposed ferroxidase site in both, as indicated by sequence analyses (Figure 1). Through kinetic and structural investigations, we completed initial characterization of recombinant *C. elegans* FTN-1 and FTN-2 proteins. Validation of the recombinant protein as a suitable model for future *in vivo* studies was verified by comparison of the kinetic parameters of recombinant ferritins with natively purified ferritins from *C. elegans*.

Materials and methods

Plasmids. The pET-21a plasmids containing the *E. coli* optimized *ftn-1* and *ftn-2* genes with the Strep-tag gene sequence, inserted between the restriction sites BamHI and NdeI were purchased from Genscript®. The Strep-tag was removed from the original plasmid sequence

through mutagenesis using the primers listed in Table S1. The human ferritin heavy chain (HuHF) cDNA was a gift from Dr. Abdel Ali Belaidi (*Florey Institute of Neurosciences and Mental Health, Melbourne*) and human ferritin light chain (HuLF) cDNA purchased from GeneCopoeia (Ex-10497-B02). From this, a plasmid was constructed using pReceiver-B02. All sequences were confirmed through Sanger-type sequencing at AGRF Ltd, Melbourne.

Expression and purification of recombinant ferritins. Rosetta-gami™ 2(DE3) competent cells (Novagen®) transformed with the plasmids encoding recombinant FTN-1 and FTN-2 were grown at 37 °C until the media reached an optical density of 0.6-0.7 at 600 nm (~3 h). FTN-1 and FTN-2 expression was induced by adding 0.3 mM isopropyl β-D-1-thiogalactopyranoside (IPTG) and incubating at 21 °C, overnight (17-18 hours). All cultures were grown in lysogeny broth (LB) media, supplemented with ampicillin (0.1 mg/mL) and chloramphenicol (0.034 mg/mL). The cells were collected by centrifugation, resuspended in buffer (50 mM Tris pH 7.8, 150 mM NaCl) with cOmplete™, EDTA-free Protease Inhibitor Cocktail and disrupted by passage through a TS series bench top cell disruptor (Constant Systems Ltd, 35 kpsi). The clarified lysate (30,000 g, 1 hour) was aliquoted (1 mL) and heat treated (80 °C, 10 mins), followed by centrifugation (15,000 g, 20 mins) to remove denatured protein. DNase I from Bovine pancreas was added to the supernatant to break down DNA and ferritin was purified by size exclusion chromatography (SEC; Superose®-6 Increase, Cytiva Life Sciences; 50 mM Tris pH 7.8, 150 mM NaCl). HuHF and HuLF were purified in a similar manner and stored at -80°C until further use. Protein purity was confirmed using sodium dodecyl sulfate-polyacrylamide gel electrophoresis (SDS-PAGE).

Protein concentration and iron content determination. Recombinant protein concentration was determined using absorbance at 280 nm using a NanoDrop™ One Microvolume UV-Vis Spectrophotometer (Thermo Scientific™). Monomer extinction coefficients of FTN-1, FTN-2 and light and heavy chain subunits of human ferritin are 17,420; 15,930; 15,930 and 19,035 M⁻¹ cm⁻¹, respectively, theoretically determined from Expasy [32]. The iron content in the protein was determined using an adapted ferrozine assay [33, 34]. Ferritin samples (5 μL) were denatured by heating with 50% (v/v) sulfuric acid (10 μL) (95 °C, 10 mins). The absorbance at 562 nm of the protein samples against a series of Fe(II) standards were measured after incubating with the ferrozine reagent (30 mins; ferrozine (5 mM), 2.86% (w/v) ascorbic acid and ammonium acetate (0.4 M)) using a microplate reader (FLUOstar Omega, BMG LABTECH).

C. elegans strains. Wild type strain N2 were obtained from the Caenorhabditis Genetics Center (University of Minnesota) and the ferritin null [*ftn-2(ok404)*; *ftn-1(ok3625)*] strain GMC005 has been previously described [9]. Strains carrying the individual ferritin null alleles were each outcrossed to wildtype four times to give GMC209 [*ftn-1(ok3625)*] and GMC210 [*ftn-2(ok404)*]. All strains were cultured at 20 °C on standard nematode growth media (NGM) supplemented with *E. coli* (strain OP50) [1].

C. elegans ferritin purification. To generate sufficient starting material, populations were maintained at scale using 8P media at 20 °C supplemented with concentrated *E. coli* (strain OP50) [35]. Every four days eggs were isolated from gravid hermaphrodite adults via an alkaline hypochlorite treatment [36]. These mixed developmental staged animals were removed from the 8P media, washed four times in excess S-basal (50 mM KHPO₄ pH 6.0, 100 mM NaCl), and briefly in ice-cold 18.2 MΩ resistant de-ionized H₂O (Millipore). Animals were frozen as pellets in liquid nitrogen and stored at -80 °C. Pellets (~ 40 g) were ground in a mortar and pestle with liquid nitrogen and homogenized in buffer (50 mM Tris pH 7.4, 150 mM NaCl, (1:1, w/v)) with cOmplete™, EDTA-free Protease Inhibitor Cocktail. The clarified homogenate (1,000 g, 10 mins) was aliquoted (1 mL) and heat treated (80 °C, 10 mins) followed by centrifugation (15,000 g, 20 mins) to remove denatured protein. The supernatant was pooled and cooled down to 4 °C to remove deposited fats before it was dialyzed (10 mM Tris pH 7.4, 15 mM NaCl) and concentrated by lyophilization. Final purification was carried out using size exclusion chromatography (Superose®-6 Increase; 50 mM Tris pH 7.8, 150 mM NaCl) and the protein was concentrated using Amicon® spin concentrators (molecular weight cut-off 100 kDa). Worm ferritin contains significant amounts of iron, which also absorb at 280 nm, so protein concentrations cannot be assessed accurately by UV-vis like recombinant protein (see below). For this reason, protein concentration was determined by gel densitometry using Bio-Rad image lab software. The yields were approximately 0.75 µg FTN-1 and 1.3 µg FTN-2/ g of worms.

Mass spectrometry. Electrospray ionization in positive mode was performed on a hybrid quadrupole time-of-flight mass spectrometer (Agilent 6520 LC/MS QTOF). Protein solutions (1 mg/mL) were injected onto a reversed-phase Jupiter® 5 µm C₅ 300 Å (50 × 2 mm) LC column through a syringe pump at a flow rate of 40 µL/min followed by protein elution using a solvent system of water and acetonitrile with 1% formic acid. The mobile phase was held at (95:5, v/v) water to acetonitrile with 1% formic acid for 5 mins where the mobile phase was

directed to waste for 3 minutes, then decreased linearly to (10:90, v/v) at $t = 15$ mins and maintained at the same gradient till $t = 16$ mins. Finally, the mobile phase was increased linearly to (95: 5, v/v) till $t = 20$ mins. Scanning was performed on a m/z range from 800-2000 and the deconvoluted spectra were obtained using the Agilent MassHunter Qualitative Analysis B.05.00 software.

Tryptic digestion mass spectrometry. The suspected stained ferritin bands from the SDS-PAGE gel were excised and destained in 50% acetonitrile with 50 mM triethylammonium bicarbonate, pH 7.8 (TEAB) (200 μ L). The gel pieces were then dehydrated in 100% acetonitrile (100 μ L) for 10 mins. The protein within the gel was digested using trypsin with an enzyme to protein ratio of 1:50 (w/w). Samples with trypsin in 50 mM TEAB buffer (pH 7.8) (40 μ L) were left at 4 °C (10 mins) for the digested peptides to diffuse and were incubated at 37 °C, overnight. Digestion was halted by addition of 1% formic acid. The Q Exactive™ Hybrid Quadrupole-Orbitrap™ Mass Spectrometer was used in positive ion mode with an ESI source. The detected peptides were analyzed by using the MS/MS search engine Byonic. Peptide masses were searched against the UniProtKB under the taxonomy of *C. elegans* incorporating a maximum of one missed cleavage site and a variable modification of methionine oxidation.

Dynamic light scattering (DLS). The hydrodynamic diameter of recombinant FTN-1 and FTN-2 were determined from autocorrelation analysis on a Horiba Nanopartica SZ-100 (Horiba Scientific, Japan), using scattered light at 532 nm with a fixed scattering angle of 90°. Three consecutive measurements of autocorrelation function for FTN-1 and FTN-2 samples of 2 mg/mL (1 mL) in buffer (50 mM Tris pH 7.8, 150 mM NaCl) were scanned for 2 minutes (each) at 25 °C. The hydrodynamic diameter was obtained from the size distribution plot using the instrument software (HORIBA-[SZ-100]).

Negative stain (NS) transmission electron microscopy (TEM) of recombinant FTN-1 and FTN-2. Recombinant FTN-1 and FTN-2 were diluted to 0.1 mg/mL and 0.5 mg/mL, respectively in buffer (50 mM Tris pH 7.8, 150 mM NaCl). Protein solution (4 μ L) was applied to glow-discharged carbon-coated 200 square mesh copper grids and allowed to incubate for 30 s (Electron Microscopy Sciences). Excess sample was wicked off and the grid was washed with Milli Q Water (4 μ L). The washed grid was incubated with uranyl acetate stain (2% w/v, 4 μ L, 30 s). Excess stain was wicked off and the grids were allowed to dry. TEM was performed

using a Talos L120C microscope equipped with a CETA 4×4k CMOS camera at 56,000× - 73,000× magnification, operating at 120 kV and pixel size of ~1.9 Å.

Cryogenic transmission electron microscopy (cryo-TEM) of recombinant FTN-2. Recombinant FTN-2 was used for single particle cryogenic transmission electron microscopy at a concentration of 10 mg/ml. Concentrated sample (4 µL) was applied to glow-discharged Cu R1.2/1.3 Holey Carbon Film grid (Quantifoil, Electron Microscopy Sciences). Grids were prepared using a Vitrobot MkIV plunge freezer (Thermo Fisher Scientific) with chamber parameters set at 22°C and 95% humidity, with a blot time of 4 secs and blot force of +1. Grids were plunge frozen in liquid ethane and stored in liquid nitrogen until use. Data were collected on a Titan Krios G4 (Thermo Fisher Scientific) operating at 300 kV with a Falcon 4 Direct Electron Detector (Thermo Fisher Scientific) A magnification of 96,000 and corresponding pixel size of 0.82 Å was used. The total electron dose was 50 e/Å².

Image processing and analysis. Image processing and analysis was carried out using CryoSPARC [37]. Micrograph movies were imported into CryoSPARC and motion corrected using the Patch motion correction implementation and CryoSPARC Patch for CTF estimation [38]. Particles were picked using Blob picker. Extracted particles were used to generate reference free 2D classes and the classes that corresponded to the expected FTN-2 molecule were selected to generate an *ab initio* 3D model.

The initial 3D maps were refined in CryoSPARC using the Gold-standard approach to a final resolution of 1.89 Å (Figure S1). Maps were inspected using UCSF Chimera. The FTN-2 crystal structure determined as part of this study was used as an atomic model template and fitted to the cryo-EM electron density map. A single FTN-2 monomer was fit to the map and octahedral symmetry applied to generate the cage-like structure. Adjustments to the template model were carried out using COOT [39] and the final 24-mer model refined using the real-space refinement tool in PHENIX [40]. Structure statistics are given in Table S2.

Stoichiometry of Fe(II) oxidation. Oxygen uptake was measured using a Clarke-type digital model-10 oxygen microelectrode (Rank Brothers Ltd.). The samples (500 µL) were pipetted into a 1 mL reaction cell with a tight-fitting stopper attached to a water circulator (Haake® model DC 10-K10) to keep the temperature constant. The oxygen electrode was calibrated by equilibrating with water (21% O₂) and addition of 200 mM sodium dithionite (0% O₂) at 20 °C. The electrode output was measured against time and the analogue voltage output was

converted by a LabTrax AD converter to digital reading. Data were acquired from the Datatrax® software. The proteins, FTN-1 and FTN-2 (2 μ M, 500 μ L) in buffer (50 mM MES pH 6.2, 150 mM NaCl, 20 °C) were equilibrated in air before specific Fe(II) /ferritin increments (3 mM $(\text{NH}_4)_2\text{Fe}(\text{SO}_4)_2$) were added and the compartment was closed.

Spectrophotometric analysis. The ultraviolet (UV)-visible spectroscopic analyses were performed using a Cary 3500 spectrophotometer (Agilent). The wavelength of maximum absorbance corresponding to the core formation in ferritin was identified by adding 96 Fe(II)/ferritin to the ferritin sample (1.7 μ M) and scanning the spectra until no further increase in absorbance was observed. The Fe(II) additions to the continuously stirred samples of FTN-1 and FTN-2 (2 μ M) in buffer (50 mM MES pH 6.2, 150 mM NaCl, 1.2 mL) were made using 12 mM $(\text{NH}_4)_2\text{Fe}(\text{SO}_4)_2$, while the absorbance was measured repeatedly at 310 nm until no further absorbance change was observed. A fresh sample of protein was used each time to measure absorbance for different increments of Fe(II)/ferritin. All added Fe(II)/ferritin increments were calculated considering the number of Fe(II) ions needed to be loaded into the ferritin 24mer.

Ferroxidase kinetic comparison between recombinant *C. elegans* ferritins and, recombinant HuHF and HuLF homopolymers was obtained (2 μ M) in buffer (50 mM MES pH 6.2, 150 mM NaCl, 1.2 mL). The absorbance at 310 nm was measured for a period of 30 minutes after the addition of 48 Fe(II)/ferritin using 10 mM $(\text{NH}_4)_2\text{Fe}(\text{SO}_4)_2$, to the continuously stirred samples.

Ferritins purified from *C. elegans* *ftn-1* null and *ftn-2* null strains (0.14 μ M and 0.06 μ M respectively) in buffer (50 mM MES pH 6.2, 150 mM NaCl, 0.6 mL) were compared against the respective recombinant ferritins under identical conditions. The activities were compared when 48 Fe(II)/ferritin 24mer were added to each sample using 1.2 mM and 1 mM $(\text{NH}_4)_2\text{Fe}(\text{SO}_4)_2$, for the corresponding FTN-1 and FTN-2 samples respectively.

Protein Crystallization and Data Collection. Initial high-throughput crystallization experiments for FTN-1 and FTN-2 (10 mg/mL, 50 mM Tris pH 7.8, 150 mM NaCl) were carried out using the Index HT screen (Hampton Research), by sitting drop vapor diffusion in 96-well plates. Crystallization drops consisting of 0.2 μ L of protein sample and reservoir solution, were established at the CSIRO Collaborative Crystallization Centre, Melbourne and drops were equilibrated against 50 μ L reservoir solution at 20°C. Crystals were observed for FTN-1 and FTN-2 in several conditions. FTN-1 condition A3 (2.0 M ammonium sulfate, 0.1

M Bis-Tris pH 5.5) and FTN-2 condition E3 (45% v/v MPD, 0.2 M ammonium acetate, 0.1 M Bis-Tris pH 6.5) were optimized by hanging drop vapor diffusion in 24-well VDX plates (Hampton Research) at 20°C. Drops consisted of equal volumes (1.0 μ L) of protein (10 mg/mL, 50 mM Tris pH 7.8, 150 mM NaCl) and reservoir solution. Diffraction quality FTN-1 crystals were observed in 1.6 M ammonium sulfate, 0.1 M Bis-Tris pH 5.0, and FTN-2 crystals observed in 34% (v/v) MPD, 0.1 M Bis-Tris pH 6.6, 0.2 M ammonium acetate. Both FTN-1 and FTN-2 crystals were flash-cooled in liquid nitrogen prior to data collection. FTN-1 crystals (FTN-1, Table S3) were soaked in cryoprotectant solution (1.7 M ammonium sulfate, 0.1 M Bis-Tris, pH 5.0, 20% (v/v) glycerol) prior to cryocooling. To facilitate phasing by multiple wavelength anomalous dispersion, an additional FTN-1 crystal was soaked in cryoprotectant containing ZnCl₂ (1.0 mM; Zn-FTN-1, Table S3).

Diffraction data were collected at 100 K on an Eiger 16 M detector at the Australian Synchrotron on beamline MX2. Data were collected from the FTN-1 and FTN-2 crystals at 13,000 eV and from the Zn-FTN-1 crystal at 9,900 eV. To locate iron binding positions in the structures, diffraction data were collected from additional FTN-1 and FTN-2 crystals at 7,000 and 7,200 eV. Diffraction data were processed with XDS [41] and merged and scaled with AIMLESS [42]. Data collection statistics are detailed in Table S3.

Structure Determination and Refinement. The FTN-2 structure was solved by molecular replacement, using the program MOLREP [43] within the CCP4 Suite [44] with a search model constructed from the coordinates of the zinc-bound ferritin from *C. variopedatus* (PDB 5WPN, [13]), modified with CHAINSAW [45]. Six copies of the search model were identified in the asymmetric unit. The structure of Zn-FTN-1 was solved using single wavelength anomalous dispersion (SAD) phasing using diffraction data collected at 9,900 eV. Analysis of these data with SHELXD [46] identified 16 Zn positions, from which phases were calculated with PHASER EP [47]. Solvent flattening with PARROT [48] yielded electron density maps into which 16 molecules of the refined FTN-2 structure could be placed using a phased molecular replacement with MOLREP [43]. A partially refined model of Zn-FTN-1 was then used to solve the FTN-1 structure by molecular replacement with MOLREP [43]. The FTN-1 and FTN-2 structures were refined using REFMAC5 [49], with twin refinement applied for the FTN-1 data set. Manual model building and the addition of water molecules were carried out in COOT [39]. NCS restraints were applied for early rounds of refinement and were released for the final

cycles. The final models show excellent geometry as determined with MOLPROBITY [50] (Table S3) and figures were generated using PyMol [51].

Results

Protein purification and characterization. Recombinant samples of the FTN-1 and FTN-2 proteins were purified with yields of 10-15 and 20-25 mg/ L of culture, respectively. SEC profiles and SDS-PAGE analyses confirmed the purity of the protein preparations (Figure 2 a)). The iron content of the recombinant ferritins as purified was determined to be 8-10 iron atoms/FTN during each purification. In contrast, the native iron core content of the FTN-1 and FTN-2 proteins, purified from *C. elegans ftn-2* and *ftn-1* null worms, respectively were determined to be 225 ± 8 and 1550 ± 40 iron atoms/ferritin (24mer).

The experimental molecular weights of ferritin monomers were determined by electrospray ionization (ESI) mass spectrometry (Figure S2 b) and c)) to yield molecular weights of 19,419.99 Da and 19,462.09 Da for FTN-1 and FTN-2, respectively. These values agree with the respective N-terminal methionyl deleted theoretical masses of 19,419.64 Da (UniProtKB ID: O16453) and 19,461.67 Da (UniProtKB ID: Q9TYS3) as calculated from the primary sequences [9]. Tryptic digested ferritin fragments extracted from SDS-PAGE gels, confirmed the sequence of FTN-1 and FTN-2 in *ftn-2* null and *ftn-1* null worm strains respectively with 83% and 87% sequence coverage through ESI mass spectrometry. DLS measurements verified the homogeneity of the FTN samples. The hydrodynamic diameters of the self-assembled 24-mer were $15.3 (\pm 0.2)$ and $14.2 (\pm 0.1)$ nm for FTN-1 and FTN-2 respectively (Figure 2 b)) [52]. Negative stain transmission electron microscopy of FTN-1 and FTN-2 samples shown in Figure S2 d) and e) also visualized individual ferritin units [13, 53].

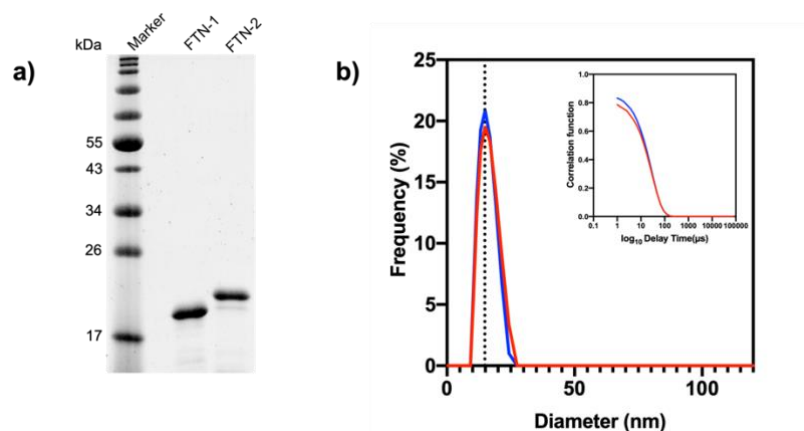


Figure 2: a) SDS-PAGE gel (15%) of FTN-1 and FTN-2 run against a molecular weight marker on the left. Molecular weights of FTN-1 and FTN-2 subunits are in the 19–20 kDa range. b) Size distribution plot of recombinant FTN-1 (red) and FTN-2 (blue) determining the hydrodynamic diameter of the self-assembled 24-

mer cage, determined through dynamic light scattering intensity data with the correlograms of FTN-1 (red) and FTN-2 (blue) in b) inset.

Structures of the FTN-1 and FTN-2 proteins. We determined the structures of the recombinant FTN-1 and FTN-2 proteins to 1.79 and 1.44 Å resolution in space groups *P23* and *I4*, respectively. The refinements converged with residuals $R = 16.8$ and $R_{\text{free}} = 19.0\%$ for FTN-1 and $R = 15.7$ and $R_{\text{free}} = 17.2\%$ for FTN-2. Cryogenic electron microscopy (cryo-EM) was also used to determine the FTN-2 structure. This resulted in a map with a global resolution of 1.89 Å (Table S2, Figure S1). All structures show excellent geometry as assessed by MOLPROBITY [50] (Table S3).

The FTN-1 and FTN-2 crystal structures and the FTN-2 cryo-EM structure all show monomers with the typical four-helical bundle folds previously described for ferritins (Figure 3). The four helices are comprised of residues 10-39 (H1), 45-72 (H2), 92-120 (H3) and 123-154 (H4), with an additional, short C-terminal helix (residues 158-169) (Figure 3a)). FTN-1 crystallized with 16 monomers in the asymmetric unit, the superposition of which yields an average root mean squared deviation (r.m.s.d) of 0.13 Å over 168 common C α positions. FTN-2 crystallized with six monomers in the asymmetric unit, the superposition of which yields an average r.m.s.d. of 0.05 Å over 168 common C α positions, indicating all protomers in the asymmetric unit of each structure are very similar. A search of the Protein Databank (PDB) [54] with the coordinates of the FTN-1 and FTN-2 monomers revealed the structures to be most like ferritins from the blood clam *Tegillarca granosa* (PDB 6L56, unpublished) and the marine invertebrate worms *Dendrorhynchus zhejiangensis* (PDB 7EMK, [55]) and *Phascolosoma esculenta* (PDB 6LPE, [56]).

Both FTN-1 and FTN-2 assemble into spherical cage-like structures composed of 24 protomers, with overall 432 symmetry. Pairs of monomers associate to form antiparallel dimers (Figure 3b)), the interaction being mediated primarily by a long loop that connects the H2 and H3 helices. This interface shows buried average surface areas of 1360 and 1394 Å² per monomer for FTN-1 and FTN-2, respectively. These dimers then interact with neighboring dimers, which are rotated at approximately 90°. There are two interfaces per monomer: (i) the N-terminus and the loop between H3 and H4 interface with H4 of the neighboring monomer (average buried surface areas of 688 and 640 Å² for FTN-1 and FTN-2, respectively) and (ii) the loop between H1 and H2 and the C-terminus of one monomer interface with H4 and the C-

terminus of another (buried surface areas of 579 and 542 Å² for FTN-1 and FTN-2, respectively). This pattern continues for assembly of the spherical structure. The superposition of the FTN-1 and FTN-2 24-mers yields an r.m.s.d. value of 0.29 Å for 1082 common C α positions, indicating the assemblies are highly conserved between the two structures. This correlates with the high sequence identity for the two proteins at 79% (Figure 1).

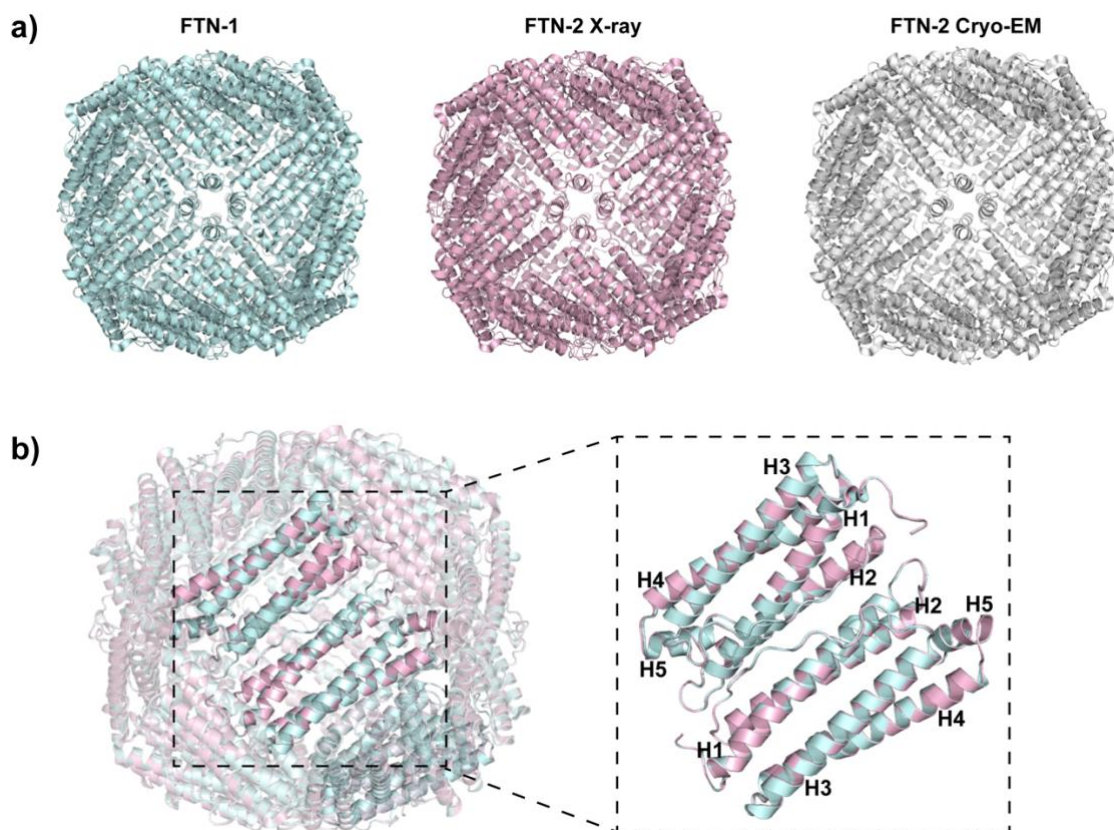


Figure 3: Overall structures of recombinant FTN-1 and FTN-2. a) FTN-1 crystal structure (light cyan), FTN-2 crystal structure (light pink) and FTN-2 cryo-EM structure (white) viewed from above the four-fold pore. b) Superposition of the FTN-1 and FTN-2 X-ray crystal structures. An antiparallel dimer is shown with helices numbered H1-H5 from the N- to the C-terminus.

Iron coordination: the ferroxidase active site. Both the FTN-1 and FTN-2 structures were modelled with a single Fe atom per protomer at the ferroxidase active site (previously designated as Fe_A in human heavy chain ferritin (HuHF)) [57], with an occupancy of 0.5. The identity of the metal as Fe (and not Zn) was confirmed by the calculation of anomalous difference Fourier maps, from data collected at 7000 and 7200 eV (Figure S3, Table S3).

In both structures, the Fe_A atom is coordinated by the side chains of Glu23 (monodentate), Glu58 (monodentate) His61 and two water molecules, which complete the 5 coordinate, square pyramidal site. These residues are conserved across practically all other ferritins. The position

of the previously characterized HuHF Fe_B site that completes the dinuclear ferroxidase center is also conserved in the FTN-1 and FTN-2 structures but does not contain iron (there was no evidence in the electron density for metal coordination). The putative Fe_B site is composed of residues Glu58 and Glu103. The observed metal stoichiometry in these structures (~0.5 Fe atoms/protomer or ~12 Fe atoms per 24-mer) approximates that determined for the recombinant FTN-1 and FTN-2 proteins as isolated (8-10 Fe atoms per 24-mer, described above).

In both FTN-1 and FTN-2, the sidechain of residue Asn106 lies in an axial position relative to the Fe_A site, facing away from the iron atom in FTN-1 (at a Fe-N distance of 3.9 Å), but pointing toward the Fe site (at a Fe-N distance of 2.5 Å) in FTN-2 (Figure 4). In the structure of FTN-2 determined by cryo-EM, both orientations of this sidechain are observed. These observations taken together, indicate flexibility in the orientation of this residue. The residue at this position has not typically been assigned as an iron ligand in other ferritin structures and lies beyond what would normally be an acceptable coordination distance in both the FTN-1 and FTN-2 proteins. In HuHF and homologous structures from invertebrates, such as the ferritins from *Tegillarca granosa* (PDB 6L56, unpublished), *Dendrorhynchus zhejiangensis* (PDB 7EMK, [55]) and *Phascolosoma esculenta* (PDB 6LPE, [56]), the equivalent residue is a valine. However, the ferritin from the marine pennate diatom *Pseudo-nitzschia multiseriata* (PmFTN) also shows an Asn residue in this position.

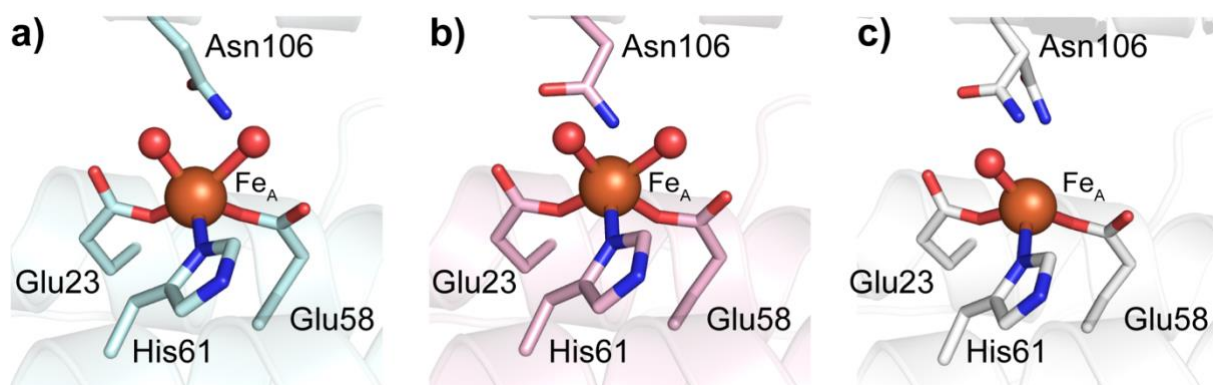


Figure 4: The residues forming the catalytic ferroxidase centers are conserved between FTN-1 and FTN-2. Ferroxidase centers of a) FTN-1, b) FTN-2 from the X-ray crystal structures and c) FTN-2 from the cryo-EM structure. One Fe ion is bound in each ferroxidase center at the Fe_A position and is coordinated by His61, Glu23, Glu58 and two water molecules. Only one water molecule is observed in the FTN-2 cryo-EM structure. Asn106 adopts an outward-facing conformation in the FTN-1 X-ray crystal structure, and an inward-facing conformation in the FTN-2 X-ray crystal structure. Both conformations are observed in the FTN-2 cryo-EM structure.

Stoichiometry of Fe(II):O₂. The oxygen consumption curves for oxidation of Fe(II) with different Fe(II)/ferritin ratios for both FTN-1 and FTN-2 are plotted in Figure 5 a) & b). The

Fe(II)/O₂ stoichiometry was obtained at O₂/Fe(II) ratios above 1 to ensure the complete oxidation of the added Fe(II). The oxidation reactions resulted in a Fe(II):O₂ stoichiometry of 2:1 upon addition of 6:1 Fe(II)/ferritin and gradually increased to saturate at a value of 4:1 at Fe(II)/ferritin ratio of >48:1 (Figure 5 c)), as previously reported for eukaryotic heavy chain ferritin homopolymers [15]. This change in stoichiometry with added Fe(II), is an indication of a change in oxidation mechanism from oxidation through the ferroxidase center alone which produces H₂O₂ through incomplete reduction of dioxygen, to involvement of peroxide mediated oxidation at a possible third site (Fec) as Fe(II) concentrations increase [15, 26, 58].

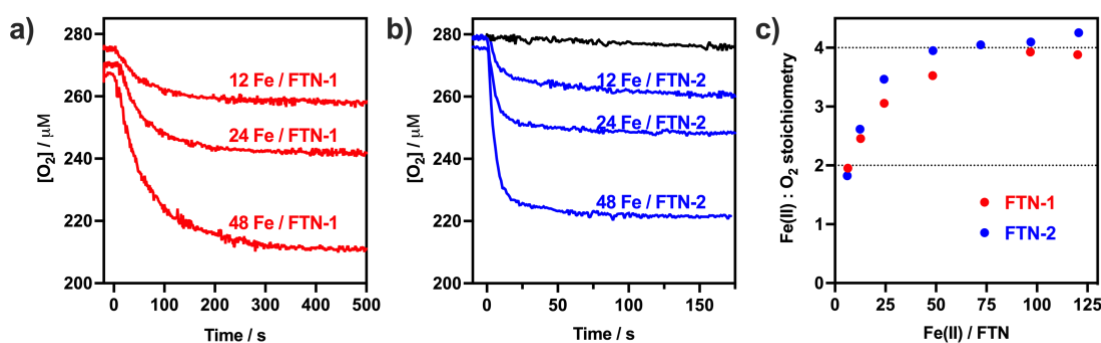


Figure 5: Oxygen consumption with time for a) and b) for 12, 24 and 48 additions of Fe²⁺/ ferritin to a fresh sample of FTN-1 (red) and FTN-2 (blue) (both 2 μ M, as isolated with 8-10 Fe atoms/ferritin) in 50 mM MES pH 6.2, 150 mM NaCl at 20 °C. c) Change in stoichiometry of recombinant FTN-1 (red) and FTN-2 (blue) against the loaded amount of Fe(II). The plot was derived from the oxygen consumption plots of FTN-1 and FTN-2 (2 μ M).

Stoichiometry of iron binding and oxidation. Under atmospheric conditions, iron added to ferritin causes large changes in the electronic absorption spectrum over time. The absorption change measured between 300-350 nm results from oxidation of Fe(II) and hence can be used to monitor the oxidation process from the beginning of the reaction through to iron core formation [59]. The ferroxidase rates of *C. elegans* recombinant ferritins with variable amounts of Fe(II) added were measured at 310 nm (Figure 6a)). These time dependent absorbance changes for both FTN-1 and FTN-2 are multiphasic and initially show a rapid increase in absorption that finishes with the formation of the μ -oxo-bridged diferric species, indicated by a plateau in absorption (Figure 6 b) & c)). This absorption change was measured for different ferrous iron additions and plotted against the ratio of Fe(II)/ferritin (Figure 6 d)). This graph was linear for both FTN-1 and FTN-2 with a discontinuity observed at 48 Fe(II)/FTN which occurs when the dinuclear iron sites in all 24 subunits of the homopolymers are occupied. Below this ratio, the slope provides the extinction coefficients (per iron) for the μ -oxo-bridged diferric species formed at the ferroxidase center. For FTN-1 and FTN-2 the extinction

coefficients were quantified to be 2430 (± 40) and 2670 (± 10) $M^{-1} \text{ cm}^{-1}$ per iron, respectively and are within the range of values previously reported [15].

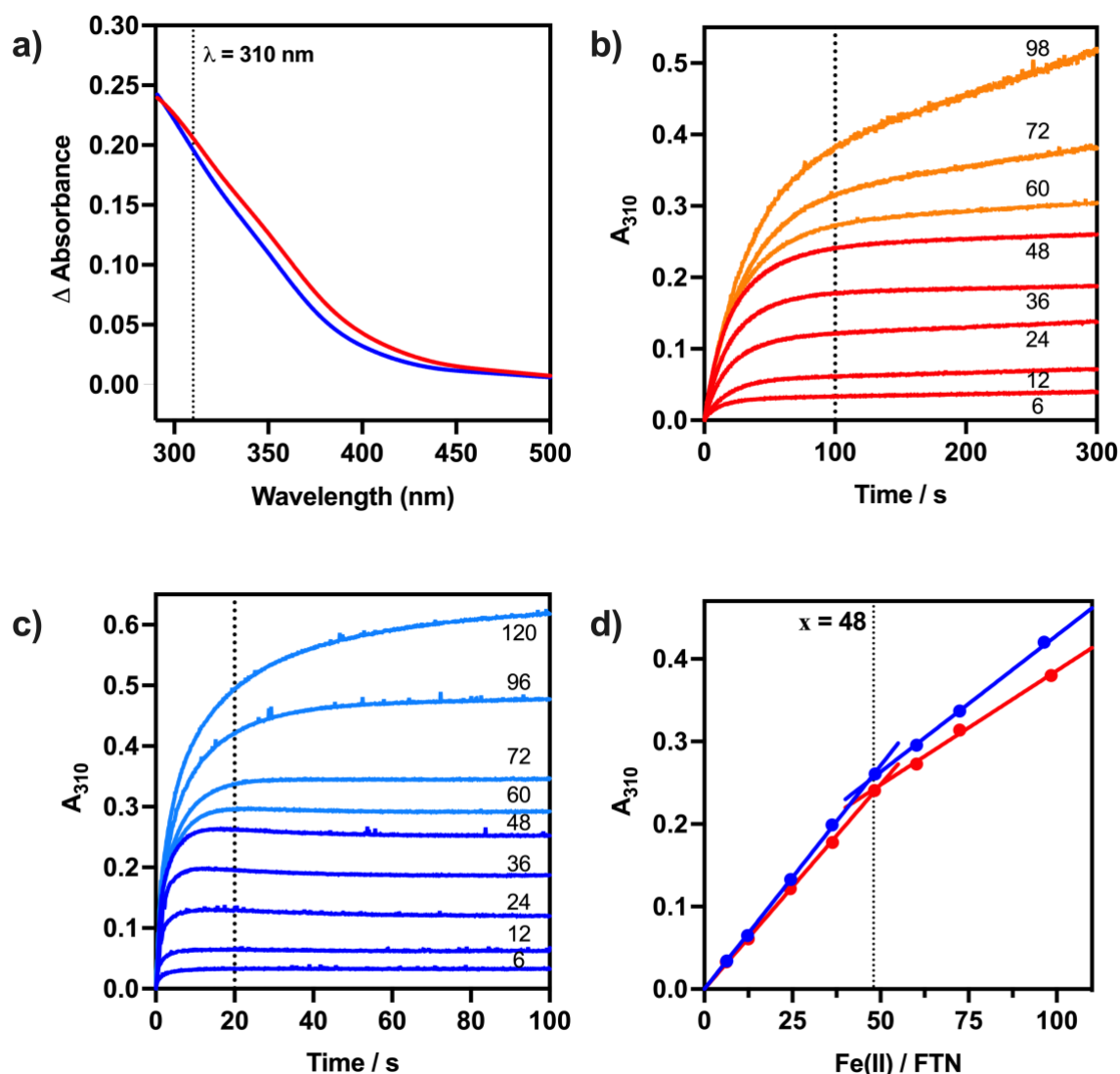


Figure 6: a) Difference in absorbance spectra for an iron loading of 48 Fe^{2+} /FTN to recombinant FTN-1 (2 μM , red) and FTN-2 (2 μM , blue) to ascertain the wavelength of maximum absorbance. Iron oxidation monitored at 310 nm against time, for different iron loadings from 6–98 Fe^{2+} /FTN-1 (2 μM , b) and 6–120 Fe^{2+} /FTN-2 (2 μM , c). Titrations were carried out in 50 mM MES pH 6.2, 150 mM NaCl at 20 °C. d) A_{310} values at the time when absorbance just starts to plateau with 48 $\text{Fe}(\text{II})$ /ferritin, plotted against iron loadings for recombinant FTN-1 (red) and FTN-2 (blue).

Kinetics of iron oxidation. The kinetics of the ferroxidase reaction were followed at 310 nm and compared with heavy and light chain homopolymers of recombinant human ferritin (HuHF and HuLF) and with ferritin purified from *C. elegans*. In Figure 7, the ferroxidase kinetics of recombinant FTN-1, FTN-2, HuHF and HuLF are compared over both short- and long-time scales. The kinetic profiles for the reaction of 48 Fe /ferritin over the initial 10 seconds are

compared and show comparable rates for FTN-2 and HuHF, approximately 10-fold slower rates for FTN-1 and a negligible rate for HuLF (Figure 7a)).

Over longer time periods (Figure 7b)), FTN-1 and FTN-2 deviate in their profile compared to HuHF and exhibit almost linear increases in absorbance that are more reminiscent of HuLF. For FTN-2, this slow increase in absorbance starts at ~80 s and follows a decrease in absorbance after the initial 10 s increase that indicates complete formation of the μ -oxo-bridged diferric species. The distinctly separated phase in the long-time scale, not only exists with Fe(II) additions above saturation of the ferroxidase sites, but at all sub-stoichiometric levels of Fe(II) additions too (Figure 7c)). This phenomenon, which has been previously recorded with ferritin from *Pseudo-nitzschia*, a marine diatom [28], is not observed in HuHF except for Fe(II) additions above saturation of the ferroxidase sites. Thus, this increase in absorbance at this latter part of the kinetic plot of FTN-2 is indicative of something occurring after the formation of the μ -oxo-bridged diferric species and could be due to iron-core formation. Similar but slower kinetics were also observed with FTN-1 but without a distinct separation between the fast ferroxidase reaction and a slower phase in the long-time scale that we believe is due to iron core formation.

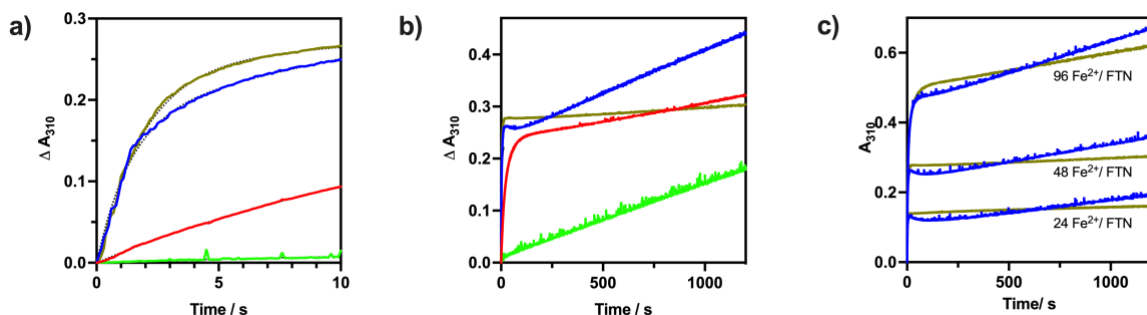


Figure 7: Differences in kinetics observed between recombinant FTN-1 (red), FTN-2 (blue), HuHF (dark green) and HuLF(light green) homopolymers by monitoring absorbance at 310 nm with time for a) the initial 10 seconds used to obtain rates of oxidation and b) a longer time scale of 20 mins c) a comparison of the absorbance profiles between FTN-2 (blue) and HuHF (dark green) for the indicated Fe / ferritin. All measurements carried out in 50 mM MES pH 6.2, 150 mM NaCl at 20 °C.

The ferroxidase activities of ferritins purified from the *C. elegans* strains, *ftn-1* null and *ftn-2* null were also compared against the activities of the respective recombinant ferritin homopolymers (Figure 8 a) & b)), to validate the recombinant ferritin models being used for kinetic and structural studies. Although quite similar, there are differences in the initial rates between recombinant and natively purified ferritins. These differences may be explained by two factors i) iron content and ii) phosphate content.

The ferritins purified from *C. elegans* strains were from a mixed stage culture which included different developmental stages and adult ages. Moreover, due to unrestricted iron levels in the growth media used, the purified ferritins resulted in considerably higher amounts of stored iron compared to the respective recombinant ferritins (see above). The quantified average amounts of iron atoms will almost certainly result from a range of core sizes and this will have contributed to the slightly altered rates of ferroxidase kinetics [58].

Additionally, analysis of ferritins from many different species indicates the presence of phosphates in the core [60, 61]. The presence of phosphate accelerates the rate of Fe(II) oxidation in the protein from *Pyrococcus furiosus* and influences the displacement of the μ -oxo-bridged diferric species in the ferroxidase center by the incoming Fe(II) [11]. Loading ~ 1550 Fe (II)/FTN-2 to recombinant FTN-2 to match with the average amount of stored iron in FTN-2 purified from *C. elegans* increased the absorption but did not produce a similar spectrum. A similar reaction in the presence of phosphate showed differences in the absorption spectrum with an increased absorbance around 310 nm that still did not exactly match but looked more comparable (Figure 8 c)). It thus appears that iron and phosphate could account for the differences observed in the rate of the ferroxidase reaction of ferritins purified from *C. elegans* to the respective recombinant ferritins.

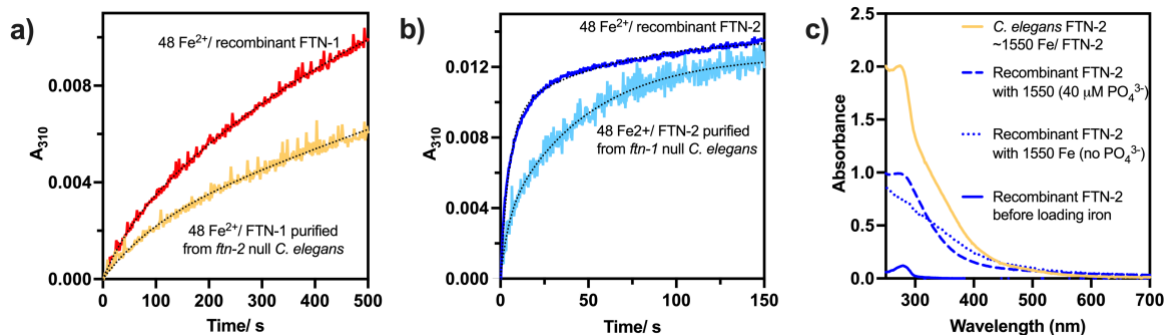


Figure 8: Comparison of kinetics at 310 nm after the addition of 48 Fe²⁺/FTN a) between FTN-1 purified from *C. elegans* (*ftn-2* null) which contains an average of 225 ± 8 iron atoms/ FTN-1 and recombinant FTN-1 which contains an average of 9 ± 1 iron atoms/FTN-1, and b) between FTN-2 purified from *C. elegans* (*ftn-1* null) which contains an average of 1550 ± 40 iron atoms/FTN-2 and recombinant FTN-2 which contains an average of 9 ± 1 iron atoms/ FTN-2. These kinetics of FTN-1 ($0.06 \mu\text{M}$) and FTN-2 ($0.13 \mu\text{M}$) were performed in 50 mM MES pH 6.2, 150 mM NaCl at 20 °C. c) Absorbance spectra of FTN-2 purified from *C. elegans* (*ftn-1* null, yellow) which had a native iron core of ~ 1550 Fe(II) /FTN-2. This is compared with spectra of recombinant FTN-2 as purified (blue) and loaded with equivalent amounts of iron in the presence (dashed blue) and absence (dotted blue) of $40 \mu\text{M}$ phosphate.

Involvement of Asn106 in FTN-2 iron coordination. The interaction of Fe_A with Asn106 was studied through site-directed mutagenesis. The asparagine residue was substituted by valine,

the conserved residue in the majority of ferroxidase active ferritins, including HuHF. The ferroxidase reaction of the variant N106V-FTN-2 was measured and compared with FTN-2. Difference spectra before and after addition of 48 Fe/FTN (1000 s) showed similar absorption with different intensities (Figure 9 a)). Indeed, the kinetic profiles measured at 310 nm were very different (Figure 9 b) and c)). Although the initial reaction over 2 s looked identical, the longer timescales showed a marked deviation. The lack of a maximum absorption at ~10 s and a less pronounced linear section at times >500 s, support the hypothesis that the oxidation and iron transfer steps are affected by Asn106. These differences will be explored in future studies.

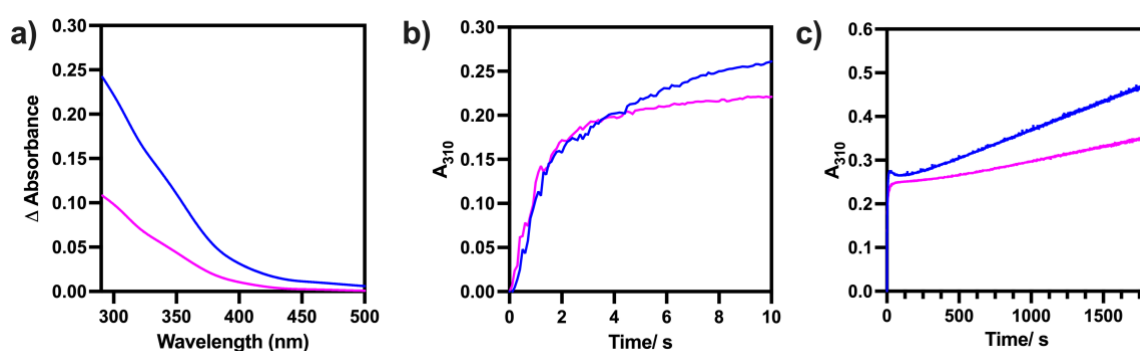


Figure 9: a) Difference in absorbance spectra after 1000s for an iron loading of 48 Fe²⁺/ FTN to recombinant FTN-2 (blue, 2 μ M) and N106V FTN-2 (pink, 2 μ M). In both cases, samples contained 8-10 Fe atoms/ ferritin. The absorptions are identical showing Asn106 does not coordinate the initial di-iron complex. Iron oxidation was monitored at 310 nm against time, for an iron loading of 48 Fe²⁺/ FTN for recombinant FTN-2 (blue, 2 μ M) and N106V FTN-2 (pink, 2 μ M) and represented for b) short and c) long time scales. Titrations were carried out in 50 mM MES pH 6.2, 150 mM NaCl at 20 °C.

The three and fourfold channels. The eight threefold channels within the tetraicosameric structure, proposed in previously studied ferritins to be involved in the entry of iron ions into the ferritin molecule, are conserved in the FTN-1 and FTN-2 structures. The pores are formed by helices H3 and H4 from three adjacent dimers, with the C-termini of H3 and the N-termini of H4 defining the outer and inner entrances of the pore, respectively. For both FTN-1 and FTN-2, the pore is lined by residues 115-131, which show sequence variations between the two proteins. Residue Glu118 in particular, which defines the ‘mouth’ of the channel in FTN-1 is a Gly residue in FTN-2. In FTN-1 Glu118 protrudes into the channel entrance, so this sequence difference accompanies a significant difference in the size of the channel entrance between these two structures (Figure 10a)). Residues 127 and 130 sit at the base of the channel in both structures, but show different charges, being Asn and Gln residues in FTN-1 and Asp and Glu residues in FTN-2, respectively. This creates a condensed electronegative charge in this region

in FTN-2, which is less prominent in FTN-1. These two features combined – a more open entrance to the channel and condensed negative charge at the base – may contribute to more rapid uptake of iron into FTN-2 than FTN-1 (Figure 10b)).

Six fourfold channels, which are proposed to provide an exit route for protons generated by the ferroxidase activity of the enzyme [62, 63], lie on the four-fold symmetry axis of the FTN-1 and FTN-2 24-mers and are bordered by the small C-terminal helix from each monomer. Residues 158, 162 and 166 line the pore. There is a charge gradient from the inside to the outside of the pore, moving from a negative charge at the base, contributed by residue Glu166 (in both FTN-1 and FTN-2) to a neutral charge at the surface. The surface residues are Leu 158 and Leu 162 in FTN-1 and Val158 and Val162 in FTN-2, therefore the surface opening of the pore is different in the two structures.

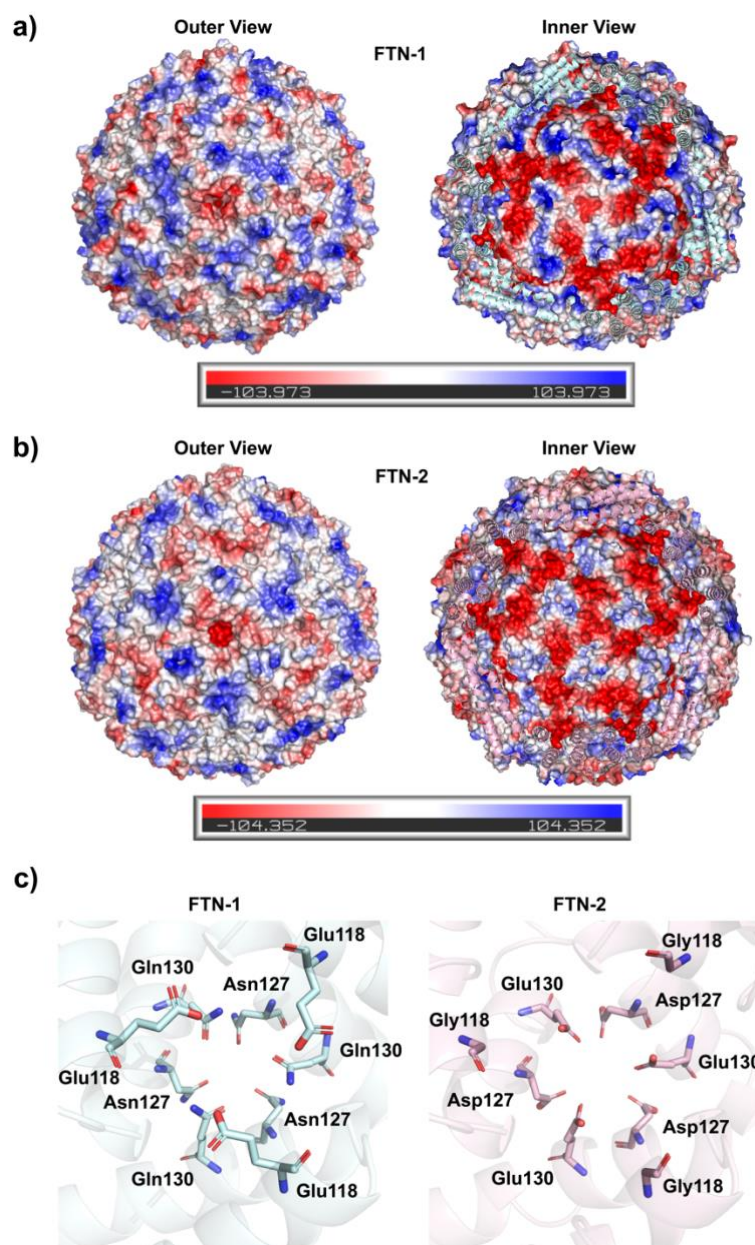


Figure 10: Electrostatic surface representations of the structures of a) FTN-1 and b) FTN-2, showing the 3-fold pore from the inner and outer views of the spherical structures. The surfaces are colored according to electrostatic potential, with red representing more electronegative regions and blue representing more electropositive regions. c) shows the amino acids that create the entrance to the 3-fold channel indicating the differences in charge and size of the entrance to both ferritins.

Discussion and Conclusion:

The two forms of ferritin from *C. elegans*, FTN-1 and FTN-2 were suspected to be ferroxidase active through comparison of their protein sequences with known ferroxidase active ferritins (Figure 1). This study has shown both recombinant and purified proteins from nematodes are indeed ferroxidase active. Measurement of changes in the UV-vis at 310 nm while adding different ratios of iron to recombinant ferritin show that a maximum of 48 iron atoms bind to the ferroxidase sites of both FTN-1 and FTN-2 (Figure 6). This corresponds to two iron atoms

binding per monomer in a di-iron ferroxidase active site. Oxygen electrode data showed that the stoichiometry of iron to oxygen reduction is 2:1 at low iron to ferritin ratios, indicative of equation 1 and the ferroxidase reaction occurring (Figure 5).



FTN-2 reacts approximately ten times faster than FTN-1 and at a similar rate to human heavy chain (HuHF) ferritin. Both oxygen electrode and UV-vis kinetics confirm this. Likewise, similar differences in rates are observed between FTN-1 and FTN-2 purified from *C. elegans*. The active sites of HuHF, FTN-1 and FTN-2 are similar, and in fact FTN-1 and FTN-2 have identical active sites. This suggests that other factors are responsible for the differences in reaction rates we observe. The transfer of iron to the ferroxidase site on the inside of the protein shell via the 3-fold channels is one process that could cause differences in reactivity. The structural comparison of the 3-fold channel shows a more open entrance and more condensed negative charge at the base of the pore in FTN-2 (Figure 10 above). We propose that this allows faster movement of iron into the ferroxidase active site in FTN-2, explaining the large differences in reactivity we observe. A similar argument has been made for the even faster ferroxidase active ferritin from the marine worm *Chaetopterus sp.* [13].

The other main difference in reactivity between the ferritins of *C. elegans* and human HuHF is the transfer of iron into the core. Over long time periods (> 250 s), the absorption at 310 nm increases linearly in FTN-1 and FTN-2. This reactivity is reminiscent of human L ferritin, which lacks ferroxidase active sites. In this case the oxidation process (following Fe(II) entry through the 3-fold channel) occurs at specific nucleation sites, which subsequently grow into a mineral core [19, 64]. Evidence of this inner surface oxidation process in HuLF was reported through identification of a tri-iron(III) species by X-ray crystallography that forms at the proposed nucleation site [21, 22], which is not present in HuHF. Apart from the Glu60 residue in HuLF, which is an Asp56 in FTN-2, identical residues aligning with the HuLF nucleation site can be identified in FTN-2 (Figure 1). We therefore propose that FTN-1 and FTN-2 have both HuHF and HuLF characteristics.

The crystal structures of FTN-1 and FTN-2 show that Asn106 is close to the ferroxidase site. In contrast, this residue is a valine in HuHF. Asn is an unusual residue in that position of the active site of ferritins but has been observed in the well characterised *Pseudo-mitzchia multiseries* ferritin PmFTN. Several crystal structures of PmFTN have been reported and

determined under different metal soaking conditions [28, 65, 66]. In all structures, the positions and orientations of the Asn97 residue (equivalent to FTN-1 and FTN-2 Asn106) are very similar, despite different metal occupancies of the ferroxidase site, and consistent with that observed for the FTN-1 structure described here. For PmFTN soaked anaerobically with ferrous iron for 75 min (PDB 4ITW, [28]) Fe is modelled at site Fe_A only (at an occupancy of 0.5) and the Asn97 O-Fe distance is 4.3 Å. The structure of PmFTN soaked aerobically with ferrous iron for 4 hours (PDB 4ISP, [28]) shows metal occupancy at sites Fe_A, Fe_B and Fe_C, with a bridging water molecule (oxygen atom) modelled between the Fe_A and Fe_B sites, which lies within hydrogen-bonding distance of the side chain of Asn97 (Asn97 N-Fe is 2.6 Å).

Interestingly, to our knowledge the role of this residue in the function and spectroscopic properties of PmFTN has not yet been addressed. It is possible that a similar interaction involving Asn106 exists in FTN-1 and FTN-2 upon full occupation of the ferroxidase sites. We assessed the importance of Asn106 by also investigating the ferroxidase kinetics of a N106V variant of FTN-2. The kinetics of the ferroxidase reaction are similar over the first 2s but quite different over longer time scales (> 10s). We therefore propose that Asn106 seems to be involved in transfer of the diferric (hydr)oxide into the core.

In conclusion, we have characterized the ferritins of *C. elegans*, an important model system for studying iron metabolism. This is the first step towards understanding iron transport to and from ferritin in a multi-cellular organism at the molecular level.

Acknowledgements:

This study was supported by grants from the Australian Research Council (ARC) to GM (DP180101248), to GNLJ and GM (DP200100110), and from the Victorian Government's Operational Infrastructure Support Program. MJM was supported by an ARC Future Fellowship (FT180100397). We thank the Caenorhabditis Genetics Center (CGC) supported by the US National Institutes of Health - Office of Research Infrastructure Programs (P40 OD010440) for providing *C. elegans* strains. Part of this study was carried out using the MX2 beamline at the Australian Synchrotron, which is part of ANSTO, and made use of the ACRF detector. We thank the beamline staff for their enthusiastic and professional support. Transmission electron microscopy was carried out at the Bio21 Institute Ian Holmes Imaging Centre (University of Melbourne) and the ARC Centre for Cryo-Electron Microscopy of Membrane Proteins. We thank the Centre staff for their technical support in data collection and

in image processing. We thank the Melbourne Mass Spectrometry and Proteomics Facility of The Bio21 Molecular Science and Biotechnology Institute at The University of Melbourne for the support of mass spectrometry analysis. Finally, we thank Dr. Abdel Ali Belaidi (Florey Institute of Neurosciences and Mental Health, Melbourne) for the HuHF plasmid.

Author contributions: SSMM expressed and purified proteins, collected and analyzed kinetic, spectroscopic, and mass spectrometry data and crystallized protein. TRM, HGB and EH collected and processed cryo-EM data. TRM built and analyzed the models. TRM and MJM collected diffraction data, solved, refined and analyzed the structures. GM prepared all *C. elegans* samples, GNLJ helped analyze kinetic data and together with GM oversaw the whole project. All members contributed to writing the manuscript.

Accession Codes: Protein (UniProtKB); FTN-1 (O16453_CAEEL), FTN-2 (Q9TYS3_CAEEL), HuHF (P02794), HuLF (P02792).

Supporting Information Available free of charge: This includes primers used in this study, data collection and refinement statistics, confirmation of the bound iron in the ferroxidase site and further characterization of FTN-1 and FTN-2.

References:

1. Brenner, S., *The genetics of Caenorhabditis elegans*. Genetics, **1974**. 77(1): p. 71-94.
2. Anderson, C.P. and E.A. Leibold, *Mechanisms of iron metabolism in Caenorhabditis elegans*. Frontiers in pharmacology, **2014**. 5: p. 113.
3. Kaletta, T. and M.O. Hengartner, *Finding function in novel targets: C. elegans as a model organism*. Nature reviews Drug discovery, **2006**. 5(5): p. 387-399.
4. Metzstein, M.M., G.M. Stanfield, and H.R. Horvitz, *Genetics of programmed cell death in C. elegans: past, present and future*. Trends in genetics, **1998**. 14(10): p. 410-416.
5. DeVincenzo, J.P., *Harnessing RNA interference to develop neonatal therapies: from Nobel Prize winning discovery to proof of concept clinical trials*. Early human development, **2009**. 85(10): p. S31-S35.
6. Zimmer, M., *GFP: from jellyfish to the Nobel prize and beyond*. Chemical Society Reviews, **2009**. 38(10): p. 2823-2832.
7. Kim, Y.-I., J.H. Cho, O.J. Yoo, and J. Ahnn, *Transcriptional regulation and life-span modulation of cytosolic aconitase and ferritin genes in C. elegans*. Journal of molecular biology, **2004**. 342(2): p. 421-433.
8. Romney, S.J., C. Thacker, and E.A. Leibold, *An iron enhancer element in the FTN-1 gene directs iron-dependent expression in Caenorhabditis elegans intestine*. Journal of Biological Chemistry, **2008**. 283(2): p. 716-725.
9. James, S.A., B.R. Roberts, D.J. Hare, M.D. de Jonge, I.E. Birchall, N.L. Jenkins, R.A. Cherny, A.I. Bush, and G. McColl, *Direct in vivo imaging of ferrous iron dyshomeostasis in ageing Caenorhabditis elegans*. Chemical science, **2015**. 6(5): p. 2952-2962.

10. James, S.A., D.J. Hare, N.L. Jenkins, M.D. de Jonge, A.I. Bush, and G. McColl, *φXANES: In vivo imaging of metal-protein coordination environments*. Scientific Reports, **2016**. 6(1): p. 1-8.
11. Honarmand Ebrahimi, K., P.-L. Hagedoorn, and W.R. Hagen, *Unity in the biochemistry of the iron-storage proteins ferritin and bacterioferritin*. Chemical reviews, **2015**. 115(1): p. 295-326.
12. Octave, J.-N., Y.-J. Schneider, A. Trouet, and R.R. Crichton, *Iron uptake and utilization by mammalian cells. I: Cellular uptake of transferrin and iron*. Trends in Biochemical Sciences, **1983**. 8(6): p. 217-220.
13. De Meulenaere, E., J.B. Bailey, F.A. Tezcan, and D.D. Deheyn, *First biochemical and crystallographic characterization of a fast-performing ferritin from a marine invertebrate*. Biochemical Journal, **2017**. 474(24): p. 4193-4206.
14. Bradley, J.M., G.R. Moore, and N.E. Le Brun, *Diversity of Fe²⁺ entry and oxidation in ferritins*. Current Opinion in Chemical Biology, **2017**. 37: p. 122-128.
15. Yang, X., Y. Chen-Barrett, P. Arosio, and N.D. Chasteen, *Reaction paths of iron oxidation and hydrolysis in horse spleen and recombinant human ferritins*. Biochemistry, **1998**. 37(27): p. 9743-9750.
16. Dickey, L.F., S. Sreedharan, E. Theil, J.R. Didsbury, Y. Wang, and R. Kaufman, *Differences in the regulation of messenger RNA for housekeeping and specialized-cell ferritin. A comparison of three distinct ferritin complementary DNAs, the corresponding subunits, and identification of the first processed in amphibia*. Journal of Biological Chemistry, **1987**. 262(16): p. 7901-7907.
17. Galaris, D. and K. Pantopoulos, *Oxidative stress and iron homeostasis: mechanistic and health aspects*. Critical reviews in clinical laboratory sciences, **2008**. 45(1): p. 1-23.
18. Squadrito, G.L. and W.A. Pryor, *Oxidative chemistry of nitric oxide: the roles of superoxide, peroxynitrite, and carbon dioxide*. Free Radical Biology and Medicine, **1998**. 25(4-5): p. 392-403.
19. Levi, S., S.J. Yewdall, P. Harrison, P. Santambrogio, A. Cozzi, E. Rovida, A. Albertini, and P. Arosio, *Evidence of H- and L-chains have co-operative roles in the iron-uptake mechanism of human ferritin*. Biochemical Journal, **1992**. 288(2): p. 591-596.
20. Ebrahimi, K.H., P.L. Hagedoorn, and W.R. Hagen, *A conserved tyrosine in ferritin is a molecular capacitor*. ChemBioChem, **2013**. 14(9): p. 1123-1133.
21. Pozzi, C., S. Ciambellotti, C. Bernacchioni, F. Di Pisa, S. Mangani, and P. Turano, *Chemistry at the protein–mineral interface in L-ferritin assists the assembly of a functional (μ³-oxo) Tris [(μ²-peroxo)] triiron (III) cluster*. Proceedings of the National Academy of Sciences, **2017**. 114(10): p. 2580-2585.
22. Ciambellotti, S., C. Pozzi, S. Mangani, and P. Turano, *Iron biomineral growth from the initial nucleation seed in L-ferritin*. Chemistry—A European Journal, **2020**. 26(26): p. 5770-5773.
23. Tatur, J., W.R. Hagen, and P.M. Matias, *Crystal structure of the ferritin from the hyperthermophilic archaeal anaerobe Pyrococcus furiosus*. JBIC Journal of Biological Inorganic Chemistry, **2007**. 12(5): p. 615-630.
24. Stillman, T., P. Hempstead, P. Artymiuk, S. Andrews, A. Hudson, A. Treffry, J. Guest, and P. Harrison, *The high-resolution X-ray crystallographic structure of the ferritin (EcFtnA) of Escherichia coli; comparison with human H ferritin (HuHF) and the structures of the Fe³⁺ and Zn²⁺ derivatives*. Journal of molecular biology, **2001**. 307(2): p. 587-603.
25. Fetter, J., J. Cohen, D. Danger, J. Sanders-Loehr, and E.C. Theil, *The influence of conserved tyrosine 30 and tissue-dependent differences in sequence on ferritin function: use of blue and purple Fe (III) species as reporters of ferroxidation*. JBIC Journal of Biological Inorganic Chemistry, **1997**. 2(5): p. 652-661.
26. Bradley, J.M., D.A. Svistunenko, J. Pullin, N. Hill, R.K. Stuart, B. Palenik, M.T. Wilson, A.M. Hemmings, G.R. Moore, and N.E. Le Brun, *Reaction of O₂ with a diiron protein generates a mixed-valent Fe²⁺/Fe³⁺ center and peroxide*. Proceedings of the National Academy of Sciences, **2019**. 116(6): p. 2058-2067.
27. Ebrahimi, K.H., E. Bill, P.-L. Hagedoorn, and W.R. Hagen, *The catalytic center of ferritin regulates iron storage via Fe (II)-Fe (III) displacement*. Nature chemical biology, **2012**. 8(11): p. 941-948.

28. Pfaffen, S., R. Abdulqadir, N.E. Le Brun, and M.E. Murphy, *Mechanism of ferrous iron binding and oxidation by ferritin from a pennate diatom*. Journal of Biological Chemistry, **2013**. 288(21): p. 14917-14925.
29. Bou-Abdallah, F., G.C. Papaefthymiou, D.M. Scheswohl, S.D. Stanga, P. Arosio, and N.D. Chasteen, *μ -1,2-Peroxo-bridged di-iron (III) dimer formation in human H-chain ferritin*. Biochemical Journal, **2002**. 364(1): p. 57-63.
30. Maiti, R., G.H. Van Domselaar, H. Zhang, and D.S. Wishart, *SuperPose: A simple server for sophisticated structural superposition*. Nucleic acids research, **2004**. 32(suppl_2): p. W590-W594.
31. Robert, X. and P. Gouet, *Deciphering key features in protein structures with the new ENDscript server*. Nucleic acids research, **2014**. 42(W1): p. W320-W324.
32. Soshnev, A.A., B. He, R.M. Baxley, N. Jiang, C.M. Hart, K. Tan, and P.K. Geyer, *Genome-wide studies of the multi-zinc finger Drosophila Suppressor of Hairy-wing protein in the ovary*. Nucleic acids research, **2012**. 40(12): p. 5415-5431.
33. Viollier, E., P. Inglett, K. Hunter, A. Roychoudhury, and P. Van Cappellen, *The ferrozine method revisited: Fe (II)/Fe (III) determination in natural waters*. Applied geochemistry, **2000**. 15(6): p. 785-790.
34. Mandal, B., P.K. Sinha, R. Sen, and A.K. Mandal, *A comparative spectrophotometric study using ferrozine and 1, 10-ortho-phenanthroline to evaluate the iron redox ratio ($Fe^{2+}/\sigma Fe$) in glass prepared by microwave heating*. Analytical Sciences, **2016**. 32(5): p. 571-576.
35. Bianchi, L. and M. Driscoll, *Culture of embryonic C. elegans cells for electrophysiological and pharmacological analyses*. WormBook: The Online Review of C. elegans Biology [Internet], **2006**.
36. Fabian, T.J. and T.E. Johnson, *Production of age-synchronous mass cultures of Caenorhabditis elegans*. Journal of gerontology, **1994**. 49(4): p. B145-B156.
37. Punjani, A., J.L. Rubinstein, D.J. Fleet, and M.A. Brubaker, *cryoSPARC: Algorithms for rapid unsupervised cryo-EM structure determination*. Nature methods, **2017**. 14(3): p. 290-296.
38. Rohou, A. and N. Grigorieff, *CTFFIND4: Fast and accurate defocus estimation from electron micrographs*. Journal of structural biology, **2015**. 192(2): p. 216-221.
39. Emsley, P., B. Lohkamp, W.G. Scott, and K. Cowtan, *Features and development of Coot*. Acta Crystallographica Section D: Biological Crystallography, **2010**. 66(4): p. 486-501.
40. Adams, P.D., P.V. Afonine, G. Bunkóczi, V.B. Chen, I.W. Davis, N. Echols, J.J. Headd, L.-W. Hung, G.J. Kapral, and R.W. Grosse-Kunstleve, *PHENIX: a comprehensive Python-based system for macromolecular structure solution*. Acta Crystallographica Section D: Biological Crystallography, **2010**. 66(2): p. 213-221.
41. Kabsch, W., *Integration, scaling, space-group assignment and post-refinement*. Acta Crystallographica Section D: Biological Crystallography, **2010**. 66(2): p. 133-144.
42. Evans, P.R. and G.N. Murshudov, *How good are my data and what is the resolution?* Acta Crystallographica Section D: Biological Crystallography, **2013**. 69(7): p. 1204-1214.
43. Vargin, A., *MOLREP: An automated program for molecular replacement*. J. Appl. Crystallogr., **1997**. 30: p. 1022-1025.
44. Winn, M.D., C.C. Ballard, K.D. Cowtan, E.J. Dodson, P. Emsley, P.R. Evans, R.M. Keegan, E.B. Krissinel, A.G. Leslie, and A. McCoy, *Overview of the CCP4 suite and current developments*. Acta Crystallographica Section D: Biological Crystallography, **2011**. 67(4): p. 235-242.
45. Stein, N., *CHAINSAW: A program for mutating pdb files used as templates in molecular replacement*. Journal of applied crystallography, **2008**. 41(3): p. 641-643.
46. Beck, T., A. Krasauskas, T. Gruene, and G.M. Sheldrick, *A magic triangle for experimental phasing of macromolecules*. Acta Crystallographica Section D: Biological Crystallography, **2008**. 64(11): p. 1179-1182.
47. McCoy, A.J., R.W. Grosse-Kunstleve, P.D. Adams, M.D. Winn, L.C. Storoni, and R.J. Read, *Phaser crystallographic software*. Journal of applied crystallography, **2007**. 40(4): p. 658-674.
48. Cowtan, K., *Recent developments in classical density modification*. Acta Crystallographica Section D: Biological Crystallography, **2010**. 66(4): p. 470-478.

49. Murshudov, G.N., P. Skubák, A.A. Lebedev, N.S. Pannu, R.A. Steiner, R.A. Nicholls, M.D. Winn, F. Long, and A.A. Vagin, *REFMAC5 for the refinement of macromolecular crystal structures*. Acta Crystallographica Section D: Biological Crystallography, **2011**. 67(4): p. 355-367.
50. Chen, V.B., W.B. Arendall, J.J. Headd, D.A. Keedy, R.M. Immormino, G.J. Kapral, L.W. Murray, J.S. Richardson, and D.C. Richardson, *MolProbity: all-atom structure validation for macromolecular crystallography*. Acta Crystallographica Section D: Biological Crystallography, **2010**. 66(1): p. 12-21.
51. Schrödinger, L. and W. DeLano, *The PyMOL molecular graphics system, version 2.0 Schrödinger, LLC (2017)*. Google Scholar There is no corresponding record for this reference.
52. Ghirlando, R., R. Mutsikova, and C. Schwartz, *Enrichment and characterization of ferritin for nanomaterial applications*. Nanotechnology, **2015**. 27(4): p. 045102.
53. Huard, D.J., K.M. Kane, and F.A. Tezcan, *Re-engineering protein interfaces yields copper-inducible ferritin cage assembly*. Nature chemical biology, **2013**. 9(3): p. 169-176.
54. Krissinel, E. and K. Henrick, *Secondary-structure matching (SSM), a new tool for fast protein structure alignment in three dimensions*. Acta Crystallographica Section D: Biological Crystallography, **2004**. 60(12): p. 2256-2268.
55. Huan, H., Q. Jiang, Y. Wu, X. Qiu, C. Lu, C. Su, J. Zhou, Y. Li, T. Ming, and X. Su, *Structure determination of ferritin from Dendrorhynchus zhejiangensis*. Biochemical and Biophysical Research Communications, **2020**. 531(2): p. 195-202.
56. Ming, T., H. Huan, C. Su, C. Huo, Y. Wu, Q. Jiang, X. Qiu, C. Lu, J. Zhou, and Y. Li, *Structural comparison of two ferritins from the marine invertebrate Phascolosoma esculenta*. FEBS Open bio, **2021**. 11(3): p. 793-803.
57. Pozzi, C., F. Di Pisa, C. Bernacchioni, S. Ciambellotti, P. Turano, and S. Mangani, *Iron binding to human heavy-chain ferritin*. Acta Crystallographica Section D: Biological Crystallography, **2015**. 71(9): p. 1909-1920.
58. Zhao, G., F. Bou-Abdallah, P. Arosio, S. Levi, C. Janus-Chandler, and N.D. Chasteen, *Multiple pathways for mineral core formation in mammalian apoferritin. The role of hydrogen peroxide*. Biochemistry, **2003**. 42(10): p. 3142-3150.
59. Treffry, A., J. Hirzmann, S.J. Yewdall, and P.M. Harrison, *Mechanism of catalysis of Fe (II) oxidation by ferritin H chains*. FEBS letters, **1992**. 302(2): p. 108-112.
60. Treffry, A., P.M. Harrison, M.I. Cleton, W.C. de Bruijn, and S. Mann, *A note on the composition and properties of ferritin iron cores*. Journal of inorganic biochemistry, **1987**. 31(1): p. 1-6.
61. Mann, S., J.V. Bannister, and R.J. Williams, *Structure and composition of ferritin cores isolated from human spleen, limpet (Patella vulgata) hemolymph and bacterial (Pseudomonas aeruginosa) cells*. Journal of molecular biology, **1986**. 188(2): p. 225-232.
62. Douglas, T. and D.R. Ripoll, *Calculated electrostatic gradients in recombinant human H-chain ferritin*. Protein Science, **1998**. 7(5): p. 1083-1091.
63. Takahashi, T. and S. Kuyucak, *Functional properties of threefold and fourfold channels in ferritin deduced from electrostatic calculations*. Biophysical journal, **2003**. 84(4): p. 2256-2263.
64. Chasteen, N.D. and P.M. Harrison, *Mineralization in ferritin: an efficient means of iron storage*. Journal of structural biology, **1999**. 126(3): p. 182-194.
65. Marchetti, A., M.S. Parker, L.P. Moccia, E.O. Lin, A.L. Arrieta, F. Ribalet, M.E. Murphy, M.T. Maldonado, and E. Armbrust, *Ferritin is used for iron storage in bloom-forming marine pennate diatoms*. Nature, **2009**. 457(7228): p. 467-470.
66. Pfaffen, S., J.M. Bradley, R. Abdulqadir, M.R. Firme, G.R. Moore, N.E. Le Brun, and M.E. Murphy, *A diatom ferritin optimized for iron oxidation but not iron storage*. Journal of Biological Chemistry, **2015**. 290(47): p. 28416-28427.

TOC "For Table of Contents use only"

